



HAL
open science

Preferential sublimation along threading dislocations in InGaN/GaN single quantum well for improved photoluminescence

B. Damilano, Stephane Vejian, M.P. Chauvat, Pierre Ruterana, Nuño Amador-Méndez, Stéphane Collin, Maria Tchernycheva, Pierre Valvin, Bernard Gil

► To cite this version:

B. Damilano, Stephane Vejian, M.P. Chauvat, Pierre Ruterana, Nuño Amador-Méndez, et al.. Preferential sublimation along threading dislocations in InGaN/GaN single quantum well for improved photoluminescence. *Journal of Applied Physics*, 2022, 132 (3), pp.035302. 10.1063/5.0089892 . hal-03865257

HAL Id: hal-03865257

<https://hal.science/hal-03865257>

Submitted on 22 Nov 2022

HAL is a multi-disciplinary open access archive for the deposit and dissemination of scientific research documents, whether they are published or not. The documents may come from teaching and research institutions in France or abroad, or from public or private research centers.

L'archive ouverte pluridisciplinaire **HAL**, est destinée au dépôt et à la diffusion de documents scientifiques de niveau recherche, publiés ou non, émanant des établissements d'enseignement et de recherche français ou étrangers, des laboratoires publics ou privés.

Preferential sublimation along threading dislocations in InGaN/GaN single quantum well for improved photoluminescence

B. Damilano,^{1,a)} S. Vézian,¹ M.P. Chauvat,² P. Ruterana,² N. Amador-Mendez,³ S. Collin,³ M. Tchernycheva,³ P. Valvin,⁴ B. Gil⁴

¹Université Côte d'Azur, CNRS, CRHEA, Rue B. Gregory, Valbonne

²Centre de Recherche sur les Ions, les Matériaux et la Photonique, CIMAP-ENSICAEN, UMR 6252, 6 Boulevard Maréchal Juin 14050, Caen

³Centre de Nanosciences et de Nanotechnologies (C2N), UMR 9001 CNRS, Université Paris-Saclay, 10 Boulevard Thomas Gobert, Palaiseau 91120, France;

⁴Laboratoire Charles Coulomb, UMR 5221 CNRS-Université de Montpellier, F-34095 Montpellier, France

^{a)}Author to whom correspondence should be addressed

ABSTRACT

InGaN/GaN single quantum wells were grown by molecular beam epitaxy on silicon substrate onto thin AlN and GaN buffer layers. The InGaN/GaN structure is porosified using a combination of Si_xN_y nanomasking and sublimation and compared to a non-porous reference. The photoluminescence efficiency at room temperature of the porosified sample is improved by a factor reaching 40 compared to the reference sample. Plan-view and cross-section transmission electron microscopy images reveal that the remaining material is free of dislocation cores. The regions around dislocations are thus preferentially sublimated. This explains the strong photoluminescence improvement of nanoporous InGaN/GaN samples.

I. INTRODUCTION

The porosification of semiconductor materials gives another degree of freedom to adjust their characteristics and to eventually improve their properties such as the luminescence efficiency of porous Si.^{1,2} Regarding nanoporous materials based on GaN, they are currently studied due to their interest for several applications as recently reviewed in Ref. 3. For example, porous GaN can be used for hydrogen generation through water splitting,⁴ piezoelectric devices,⁵ chemical sensing⁶ or optoelectronics. Distributed Bragg reflectors composed of a stack of alternating regular GaN and nanoporous GaN demonstrated a high reflectivity and the possibility to be lattice matched on GaN.^{7,8,9,10} Such distributed Bragg reflectors can be used as highly reflective bottom mirrors in different devices including resonant cavity light emitting diodes,^{11,12} as well as optically pumped,¹³ and electrically injected vertical cavity surface emitting laser.^{14,15} Last, incorporating porous GaN layers on top of a patterned sapphire substrate can also enhance the light extraction efficiency of blue InGaN/GaN light emitting diodes thanks to the modification of the refractive index of the porous GaN.¹⁶

The porosification of GaN-based layers modifies their structural and optical properties. Transforming GaN layers into porous GaN layers has a strong impact on the strain state.^{17,18} This property was exploited to relax the compressive strain in InGaN layers located on top of porous GaN layers.¹⁹ Such an approach was applied to fabricate InGaN micro light emitting diodes with a long wavelength emissions extending up to the red.^{20,21}

The main technique used for the porosification of GaN layers is based on electrochemical etching or photo-enhanced electrochemical etching on either n-type or p-type GaN.^{22,23,24,25,26} Porous GaN layers can also be produced from initially flat GaN layers using an electroless chemical etching assisted by Pt.²⁶ Pandey et al. showed that it was possible to make porous GaN layers by the annealing of planar GaN layers covered by gold nanoparticles.²⁸ Similarly, a high temperature thermal treatment of GaN layers can be applied to induce the porosification of the layers under a H₂ atmosphere in a hydride vapor phase epitaxy reactor or a metal-organic vapor-phase epitaxy reactor,^{29,30} or alternatively under a N₂ atmosphere in a resistance furnace³¹ or eventually under vacuum in a molecular beam epitaxy reactor after the deposition of a Si_xN_y nanomask.^{32,33,34} Through this last approach, we showed that the photoluminescence efficiency at room temperature of highly dislocated GaN layers was strongly increased when they were porosified. We previously attributed this improvement to the preferential sublimation of GaN around dislocations but with only indirect elements supporting this hypothesis. In the present work we report on the optical and structural properties of an InGaN single quantum well and we directly show at the light of transmission electron microscopy experiments that after porosification the remaining GaN and InGaN layers are free of extended defects emerging at the surface.

II. EXPERIMENTAL

A. Fabrication of the samples

The samples were grown on Si(111) substrate by molecular beam epitaxy (MBE) in a Riber system. The 2-in. substrates were deoxidized *ex situ* using a diluted HF solution. Then the samples were mounted "In-free" on molybdenum holders and loaded in the MBE system. The samples were grown in two consecutive runs and the same molybdenum was used for both runs in order to ensure a good run to run reproducibility. The epitaxial stack consisted of a 95 nm AlN buffer layer, a 245 nm GaN layer, a 2 nm

InGaN quantum well and a last 25 nm GaN cap layer (Figure 1a). The procedure described in Refs. ³⁵ and ³⁶ was applied to prepare the Si for initiating the AlN growth. Solid sources were used for Al, Ga and In. Regarding nitrogen, it is provided by the thermal cracking of ammonia on the sample's surface. The temperatures were measured using an infra-red optical pyrometer and by calibrating the emissivity of the samples by considering the transition of the 7x7 to 1x1 surface reconstruction (as measured by reflection high energy electron diffraction) at 830°C. The growth temperature/ammonia flow were respectively 880°C/50sccm, 780°C/100sccm, and 540°C/500sccm for AlN, GaN, and InGaN layers. One sample was kept as a reference, while the second was processed. The porosification was carried out in two steps: the first one consisted in exposing the GaN surface to a Si flux (Si cell heated at 1250°C) for 13 minutes to generate the formation of a Si_xN_y ultrathin layer of less than 1 mono-layer (Figure 1b). It should be noted that any discontinuity of this thin Si_xN_y creates a preferential path for GaN sublimation. In the second step, the sample was heated at 880°C in an ammonia flow of 10 sccm for 64 min and then kept under vacuum for 36 min at the same temperature (Figure 1c). The Si_xN_y nanomask of the porous sample was not removed *ex situ* before the characterizations.

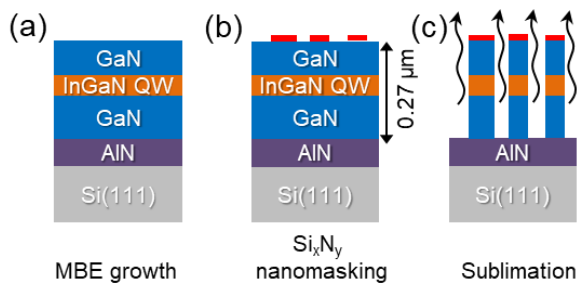


Figure 1. The different steps for the fabrication of the samples. (a) Epitaxial growth of the structure by molecular beam epitaxy. (b) Exposition of the surface to a Si flux to form a Si_xN_y nanomask. (c) Sublimation in the molecular beam epitaxy reactor at 880°C.

B. Structural characterizations

The surface and the cross-section of the samples were imaged using a Zeiss Supra 40 scanning electron microscope at an acceleration voltage of 5 kV. For transmission electron microscopy analysis, a JEOL ARM 200 was used as a scanning transmission electron microscope (STEM). The samples for plan-view and cross section measurements were prepared by focused ion beam with energies that were varied from 30 down to 1 kV for final polishing in order to minimize the beam generated damage. The thinning process was closely monitored; during the process, structural and chemical information was acquired using the electron beam first in the scanning mode, and second in the scanning transmission mode. The latter becomes possible when the lamella is thin enough for transparency to the low energy electrons (30 kV).

C. Optical characterizations

Continuous wave photoluminescence experiments were performed at room temperature and as a function of the temperature (10K-300K) in a closed-circuit He cryostat. The 244 nm line of a frequency-doubled Ar laser (Fred90C from Coherent) with a power of 30 mW was used as the excitation source. The spot size diameter was $\sim 120 \mu\text{m}$ which gave an excitation power density of 300 W/cm^2 . The

photoluminescence emitted by the samples was collected by achromatic lenses and focused to a fiber connected to an Acton SP558 spectrometer. The photoluminescence experiments on both porous and non-porous samples were performed the same day in the same measurement run, therefore the PL intensities are directly comparable.

Time-resolved photoluminescence (TRPL) spectroscopy measurements were performed as a function of the temperature in a closed-circuit He cryostat. A laser at a wavelength of 266 nm was used as the excitation source. The pulse repetition rate of the laser was chosen at 80 kHz. The emission light of the samples was recorded by a spectrometer connected to a Hamamatsu-C10910 streak camera.

CL measurements were performed at room temperature in an Attolight Chronos CL-scanning electron microscope (SEM) system. Light was collected by an achromatic reflective objective (numerical aperture 0.72) that provided constant collection efficiency over a field of view of about 150 μm in diameter. Acceleration voltage of the electron beam was set to 6 kV, and the current of approximately 2 nA was kept constant. The diffraction grating used has 150 grooves/mm and is blazed for 500 nm wavelength. The signal was recorded with an Andor Newton charge-coupled device (CCD) camera (1024x256 pixels, with a pixel width of 26 μm). The corresponding spectral dispersion is 0.53 nm per pixel. Luminescence spectra were corrected for the diffraction efficiency of the grating and the sensitivity of the CCD camera. The luminescence intensity described in the text corresponds to a spectral density of photon flux per unit of energy (counts/(s.eV)).

II. RESULTS AND DISCUSSION

A. Scanning electron microscopy

The surface of the samples is shown in the SEM images of Figure 2(a) and (b). The surface of the non-porous sample appears flat with almost no visible pits on the whole image area. On the other hand, the surface of the porous sample is affected by many pits. The minimum diameter of these pits is less than 10 nm, however it is difficult to be precise with such small dimensions in SEM imaging. A better resolution is achieved with TEM experiments that are described in the following. The maximum diameter of isolated pits is ~ 25 nm. The size of these pits indicates that we have a mesoporous material. The surface density of these pores is estimated to be $8 \times 10^{10} \text{ cm}^{-2}$. The SEM cross-section images of the samples are shown in Figure 2(c) and (d). The non-porous sample shows compact and smooth GaN and AlN layers as expected from an epitaxial growth on Si(111) using a 2-dimensional growth mode.³⁵ Regarding the porous sample, the sidewalls of the pores are vertical, perpendicular to the surface and they penetrate down to the AlN buffer layer (Figure 2(d)). This specific vertical morphology of the pores is due to the strong anisotropy of the thermal stability of the different crystallographic planes of wurtzite GaN. The GaN vertical planes, perpendicular to the surface, are much more stable under vacuum than the (0001) and therefore their sublimation rate is much smaller. The sublimation rate of the planes perpendicular to the surface was estimated to be only $\sim 1\%$ of the sublimation rate of the planes parallel to the surface.³⁷ Previously, this property was advantageously exploited for the successful top-down fabrication of GaN nanowires^{37,38,39,40} or nanoholes.⁴¹

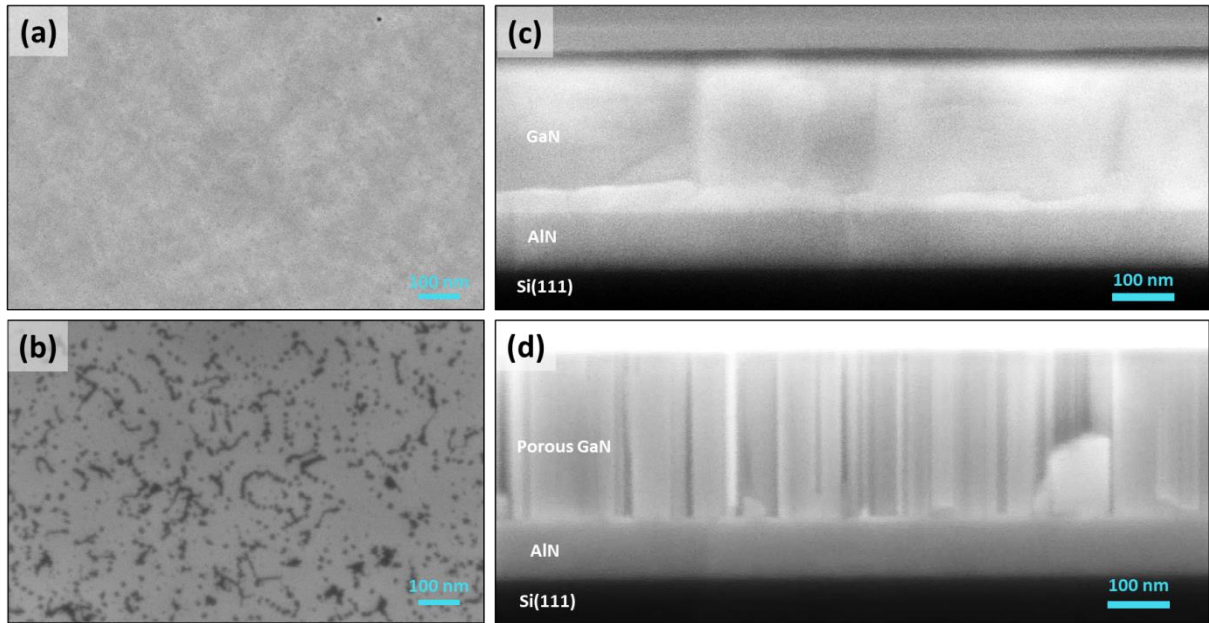


Figure 2. Scanning electron microscopy images of the surface (left) and the cross section (right) of the non porous (a)(c) and the porous (b)(d) samples. The different visible layers (Si(111) substrate, AlN and GaN) are indicated on the cross section images. The very thin InGaN quantum well cannot be clearly seen due to the limited magnification.

B. Photoluminescence and time-resolved photoluminescence

Figure 3(a) shows the room temperature photoluminescence (PL) of the non-porous and the porous InGaN/GaN single quantum well. The integrated PL intensity of the porous sample is larger by a factor of about 40 compared to the PL intensity recorded on the non-porous sample. The PL peak energy of the non-porous QW is at 2.774 eV and it is blue-shifted to 2.844 eV for the porous sample. Several effects can explain this blue-shift. It is well known that the PL properties of polar InGaN/GaN quantum wells are affected by the presence of a strong internal piezoelectric field.^{42,43} One straightforward consequence of this internal field, the quantum confined Stark effect, is the downward shift of the energy values of the fundamental e_1 - hh_1 QW transition. Indeed, the InGaN quantum well is strained onto the GaN layer for the non-porous sample. The formation of pores creates free surface in sufficient amounts to enable the elastic strain relaxation of the InGaN. The consequence of this relaxation is a decrease of the internal electric field and therefore a blue-shift of the QW transition compared to the transition energy in the non porous reference sample.⁴⁴ This shift is somewhat attenuated by the bandgap reduction of the InGaN due to the elastic relaxation (the InGaN layer is initially compressively strained on the thick GaN layer). The room temperature PL energy of the GaN band-edge is 3.410 eV for the non-porous sample and 3.407 eV for the porous one. This indicates that the strain state of GaN is almost perfectly relaxed even for the non-porous sample and does not significantly evolve when the layer is porosified. Therefore the GaN strain state does not impact the PL peak energy of the InGaN QW before and after porosification. Another reason of this blue-shift can be the In desorption from the InGaN quantum well as the surface of the InGaN layer is exposed by the creation of pores. Indeed, the decrease of the In composition can lead to the decrease of the InGaN bandgap. We remind that, a change in the localization state of the excitons in the InGaN QW could impact the PL peak energy. To investigate this possibility we measured the PL peak energy as a function of the temperature (Figure 3(b)). The variation of the PL energy for both samples is the same and this indicates that there is no

change in the localization degree in an amount susceptible to modify our interpretation of the PL peak shift due to the porosification.

Figure 3(c) shows the integrated photoluminescence intensity variation as a function of the temperature for both the non-porous and the porous samples. The ratio of the PL intensity between 300 K and 10 K are 0.007 and 0.161 for the non-porous and the porous sample, respectively. The value is very small for the non-porous sample and far from the current standards (> 0.8) for blue emitting InGaN/GaN quantum wells⁴⁵ because the structure is very thin (total GaN thickness of 270 nm) and affected by a very large density of threading dislocations (close to 10^{11} cm^{-2} , see below). The PL intensity of the porous sample is much more robust with temperature, which indicates that non-radiative recombination processes are strongly reduced for this sample. Complementary time-resolved PL experiments confirm this observation and show that the decrease of the PL decay time with temperature is smaller for the porous sample compared to the non-porous one (Figure 3(d)). The PL decay times at low temperature are 0.71 ns and 0.50 ns for the non-porous and porous sample, respectively. At low temperature, most of the non-radiative processes are frozen and therefore the PL decay time is close to the PL radiative lifetime (eventually slightly smaller). This decrease of the PL radiative lifetime can also have an intrinsic origin, it can also be explained by the reduction of the internal piezoelectric field due to the InGaN strain relaxation in the porous sample. Indeed, when the internal electric field decreases the radiative lifetime decreases.⁴³ Actually, both contributions can co-exist, which we cannot discriminate.

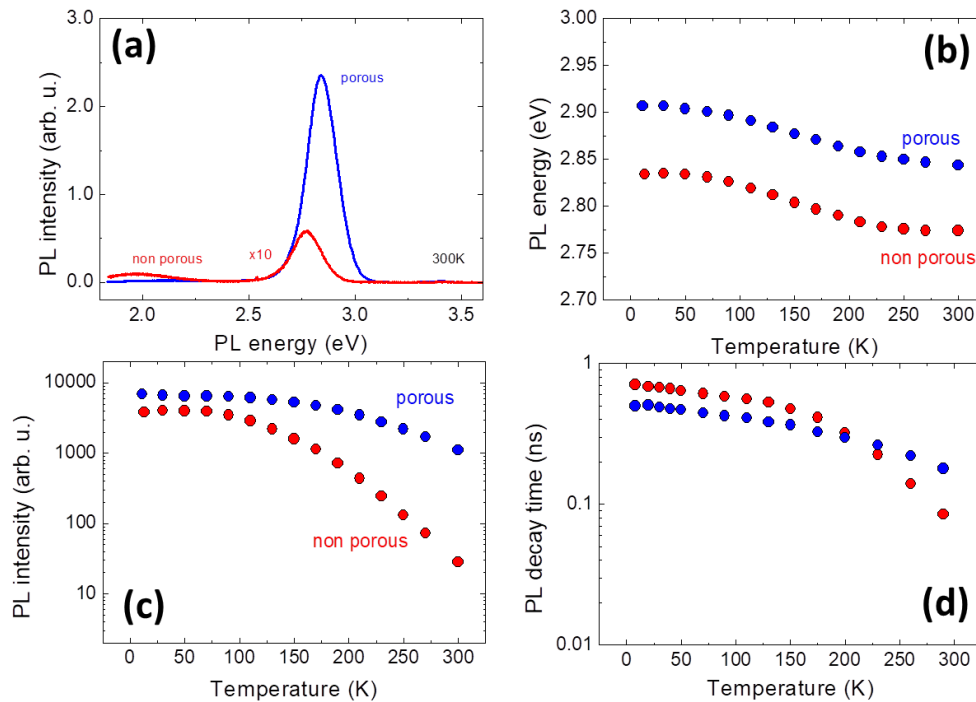


Figure 3. Comparison of the photoluminescence properties of a non porous and porous InGaN single quantum well. (a) Room temperature photoluminescence. Note that the photoluminescence intensity of the spectrum of the non-porous sample is multiplied by a factor of 10. (b) Photoluminescence peak energy as a function of the temperature. (c) Integrated photoluminescence intensity as a function of the temperature. The photoluminescence in (a),(b) and (c) is excited by a CW laser source. (d) Photoluminescence decay times as a function of the temperature.

C. Cathodoluminescence

The optical properties of these samples were studied at a more local scale using CL mapping at room temperature (Figure 4(a)-(g)). Figure 4(a) shows the normalized CL spectra of both samples integrated over the whole studied area of $2.5 \times 2.5 \mu\text{m}^2$. The same blue-shift (70 meV) as in PL is observed for the CL peak of the InGaN/GaN single quantum well of the porous sample compared to the non-porous one. The SEM images of the surface of the areas under investigation are shown in Figure 4(b) and (d) and can be directly compared to the CL energy and intensity maps of Figure 4(c)-(g). Astonishingly, as a first remark, there is no obvious coincidence between the morphology observed by SEM and the CL maps. However, there is a clear evolution of these maps between the non-porous and the porous sample.

The CL energy map of the reference (non-porous) sample (Figure 4(c)) reveals fluctuations of the quantum well emission with an average value of the spatial scale on the order of a few 100 nm^2 . The QW energy emission is relatively homogeneous inside domains with this surface area. These fluctuations can be attributed to the growth of the InGaN quantum well which can present some random variations of thickness and of In composition. We find a similar spatial scale, corresponding to a large variation of the CL energy, for the porous sample (Figure 4(f)) and, inside these domains, we can eventually record a small variation of the CL energy peak. Note that in the CL map of Figure 4(f) some pixels appear white at the position of large pores, where no QW emission is detected. The standard deviations for these maps are 10 meV and 21.7 meV, for the non-porous and porous samples, respectively. This larger value of the standard deviation for the porous sample is probably related to the fact that the strain in the InGaN quantum well can locally vary, depending on the local distribution of the pores. Indeed, the size and the distribution of the pores are not homogeneous.

The CL panchromatic intensity map of the non-porous sample (Figure 4(d)) also shows spatial fluctuations on the order of a few 100 nm^2 . For the porous sample (Figure 4(g)) the typical scale of these fluctuations becomes much smaller, i.e. on the order of a few 10 nm^2 . This is plausibly related to the porosification of the InGaN quantum well. It is clearly visible that at the position of big pores the CL intensity is very weak. The standard deviation for these CL intensity maps is 2500 (over max of 24000 (10.4%), mean of 12000) and 13500 (over max of 110000 (12.3%), mean of 38000), for the non-porous and the porous sample, respectively. Therefore a very similar standard deviation for the CL intensity is observed for both samples despite the porosification.

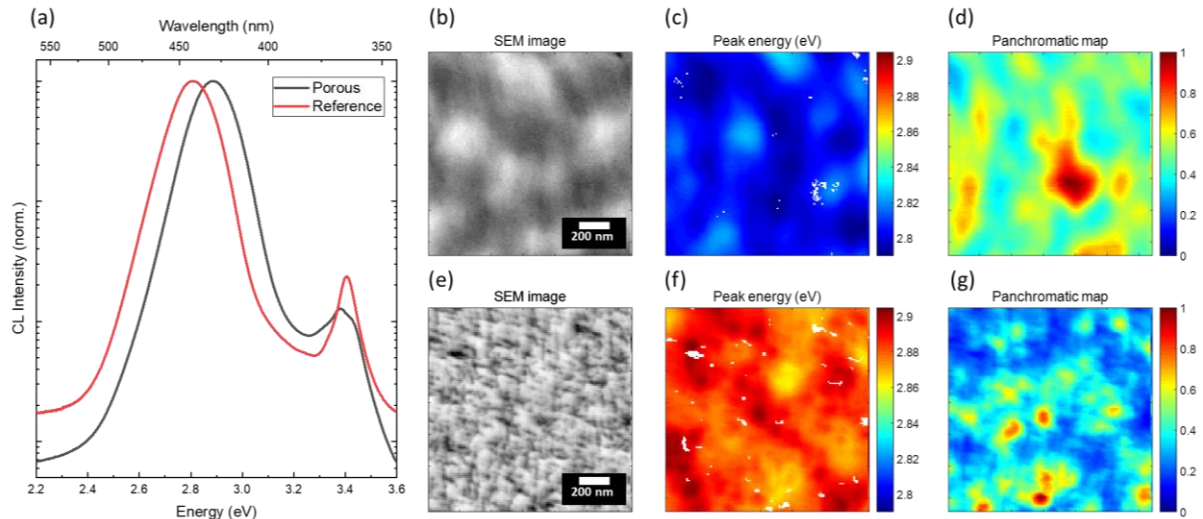


Figure 4. (a) Room temperature cathodoluminescence spectra of the non porous and porous InGaN/GaN single quantum well. The figures (b)(c)(d) and (e)(f)(g) are related to the non-porous and porous samples, respectively. The area corresponding to the figures (b)(c)(d)(e)(f)(g) is $2.5 \times 2.5 \mu\text{m}^2$. (b)(e) Secondary electron scanning electron microscopy images. (c)(f) Quantum well peak energy cathodoluminescence map. (d)(g) Panchromatic intensity cathodoluminescence map.

D. Transmission electron microscopy experiments

Figure 5 shows STEM images of the non-porous (Figure 5(a)(c)) and porous (Figure 5(b)(d)) samples. Figure 5(a) and (b) shows the plan-view STEM images of the non-porous and porous samples, respectively. These images correspond to the top GaN surface (the thickness of the specimen is around 100 nm). In the cross-section images (Figure 5 (c) and (d)), the different layers can be clearly identified: the AlN buffer layer, the GaN layer and 30 nm below the surface, the InGaN quantum well.

The non-porous sample is affected by a large density of dislocations as it is expected for thin GaN and AlN grown on Si(111) substrates. We can see numerous dislocations loops in GaN on Figure 5(c) that, at the interface with the AlN buffer layer, in the first 50 nm, lead to a reduction of threading dislocations in the upper GaN layer (and in the InGaN quantum well). From the plan-view image shown in Figure 5(a), we note that the dislocations are arranged into irregular sub-grain boundaries⁴⁵. In this large camera length STEM dark field image, the strain field which is imaged comes out mostly as continuous irregular lines due to the fact that the dislocations are too close to be resolved. In the same figure, we identify many bright individual points which are not connected to sub-grain boundaries, but are visible with contrast. We can very roughly estimate the emerging threading dislocation density as $>7 \times 10^{10} \text{ cm}^{-2}$ in this area.

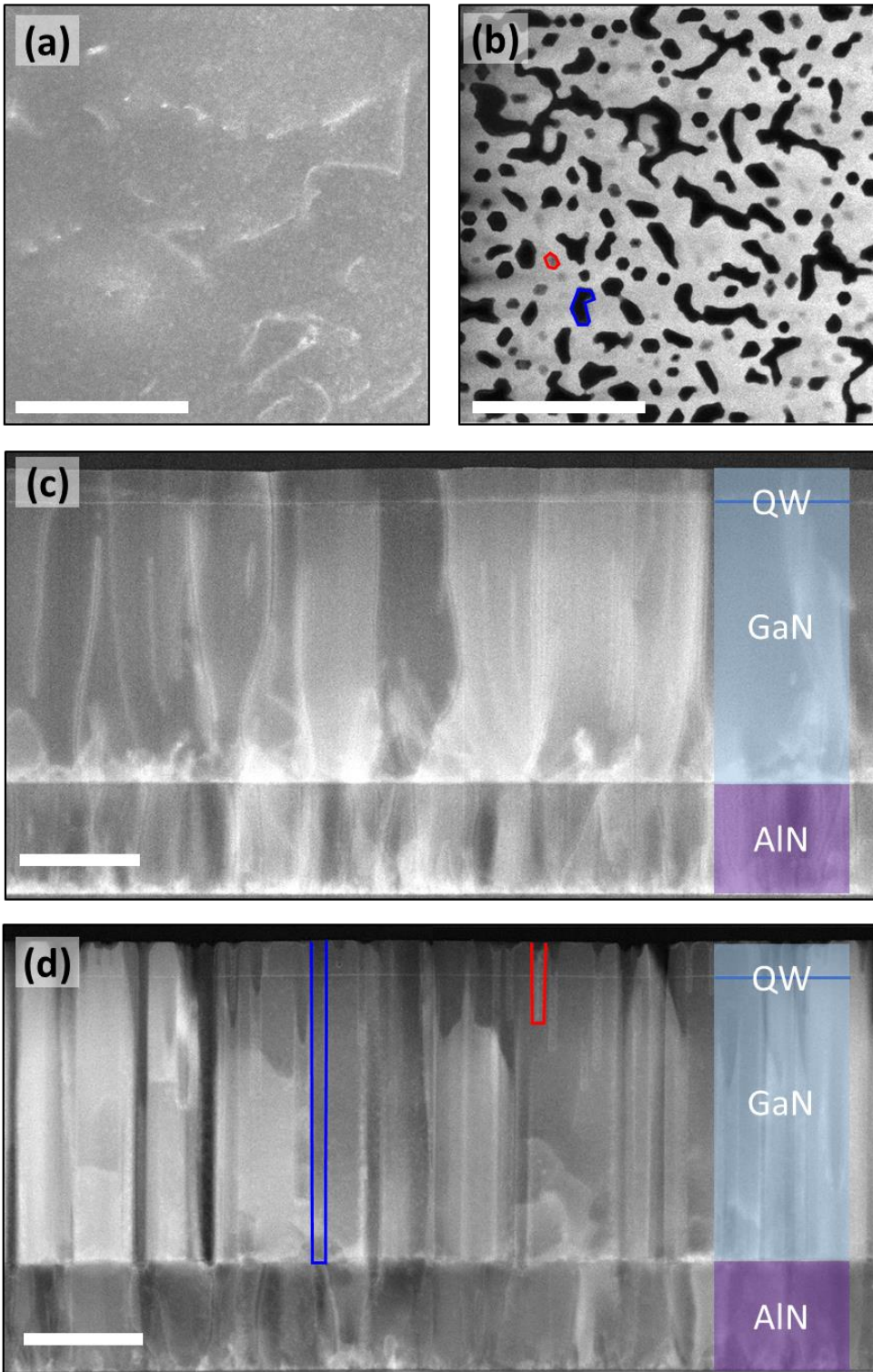


Figure 5. Plan-view (a)(b) and cross section transmission electron microscopy images along the [11-20] zone axis (c)(d) scanning transmission electron microscopy images of an InGaN/GaN quantum well on AlN/Si(111) as grown (a)(c) and after porosification by sublimation (b)(d). The regions enclosed by a red or a blue line correspond respectively to partially sublimated pores and pores extending down to the AlN buffer layer. No dislocation line can be detected below partially sublimated pores. The scale bar in 100 nm for all images.

In the plan-view TEM image of the porous sample (Figure 5(b)), no dislocations can be detected in the remaining GaN after sublimation. The pores can be seen as dark contrast areas of various shades, they exhibit different sizes and shapes. The largest ones exhibit the darkest contrast (the periphery of one of such pore is highlighted in blue in Figure 5(b)) and are irregularly elongated, which clearly indicates that they originate from the sublimation of sub-grain boundaries. Moreover, isolated areas may also be identified as darkest areas of various shapes, which can even be limited by more or less deformed hexagonal facets; their size may exceed an average diameter of 10 nm. In this image, such darkest contrast means that the corresponding areas are empty; therefore they correspond to completely sublimated regions. The density of the pores with the darkest contrast extracted from Figure 5(b) is $>1.4 \times 10^{11} \text{ cm}^{-2}$; this value is in the same order of magnitude than the threading dislocation density estimated for the non-porous reference sample. Many randomly distributed areas exhibit light-grey contrast with well-defined hexagonal facets, with an average diameter around 5 nm (one example is highlighted in red in Figure 5(b)). A close examination of the cross section image in Figure 5(d) may help to explain these features. As marked in red, sublimated areas in some cases can extend only a few tens of nanometers from the surface. In the plan view image they are partially filled by perfect GaN material since the corresponding sublimation hole does not run all the way through the TEM lamella. The systematic analysis of the dislocation content on these features does not reveal any enclosed crystallographic defect. Therefore, such contrast corresponds to partially sublimated areas without defect for which the Si_xN_y nanomask presented an aperture. The information from these observations is that all the dislocation lines have undergone sublimation all the way through down to the AlN layer. The result is that the remaining GaN material is free of emerging dislocation cores at the surface as shown on the plan-view (Figure 5(b)) and cross-sections images (Figure 5(d)). Clearly, this is a direct proof that the sublimation process preferentially occurs at the dislocation positions and all along their lines. The preferential etching of the dislocation core by electrochemical etching was previously reported and analyzed by Massabuau et al.^{47,48}

This definitely clarifies the role of the porosification by sublimation which is found to remove the non-radiative dislocation cores from the active layers and thus leads to a strongly increased radiative efficiency of InGaN quantum well and GaN layers. However, it has to be pointed out that the created pores can be a source of non-radiative recombination at their surface. This eventual issue could be evaluated using surface passivation as reported in previous works for GaN nanowires.^{49,50}

IV. CONCLUSION

This study demonstrates and clarifies the role of selective area sublimation of GaN and an InGaN/GaN QW in the presence of a large density of dislocations. Using plan-view and cross-section transmission electron microscopy, we show that the material close to dislocations emerging at the surface is preferentially sublimated which results in extended defect-free active layers. As a consequence, the room temperature photoluminescence intensity of porous InGaN/GaN QW is largely enhanced compared to a non-porous InGaN/GaN QW. This property can therefore be exploited when GaN layers are affected by a large density of extended defects to enhance their radiative efficiency.

ACKNOWLEDGMENTS

This work has been supported by the French National Research Agency (ANR) through the project NAPOLI (ANR-18-CE24-0022). For the TEM sample preparation, this work acknowledges the use of the SEM/FIB FEI Nanolab 660, which is a facility acquired in the scope the EQUIPEX GENESIS, N° ANR-11-

EQPX-0020 under the “Investissements d’avenir” national Programme. The authors would like to thank Julien Brault and Philippe Vennéguès for the critical reading of the manuscript.

AUTHOR DECLARATIONS

Conflict of Interest

The authors have no conflicts to disclose.

DATA AVAILABILITY

The data that support the findings of this study are available from the corresponding author upon reasonable request

REFERENCES

- ¹ A.G. Cullis, L.T. Canham, and P.D.J. Calcott, *J. Appl. Phys.* **82**, 909 (1997).
- ² V. Agarwal, J.A. del Río, G. Malpuech, M. Zamfirescu, A. Kavokin, D. Coquillat, D. Scalbert, M. Vladimirova, and B. Gil, *Phys. Rev. Lett.* **92**, 097401 (2004).
- ³ P.H. Griffin and R.A. Oliver, *J. Phys. Appl. Phys.* **53**, 383002 (2020).
- ⁴ J. Benton, J. Bai, and T. Wang, *Appl. Phys. Lett.* **105**, 223902 (2014).
- ⁵ J.-H. Kang, D.K. Jeong, J.-S. Ha, J.K. Lee, and S.-W. Ryu, *Semicond. Sci. Technol.* **32**, 025001 (2017).
- ⁶ A. Ramizy, Z. Hassan, and K. Omar, *Sens. Actuators B Chem.* **155**, 699 (2011).
- ⁷ J. Park, J.-H. Kang, and S.-W. Ryu, *Appl. Phys. Express* **6**, 072201 (2013).
- ⁸ C. Zhang, S.H. Park, D. Chen, D.-W. Lin, W. Xiong, H.-C. Kuo, C.-F. Lin, H. Cao, and J. Han, *ACS Photonics* **2**, 980 (2015).
- ⁹ G.-Y. Shiu, K.-T. Chen, F.-H. Fan, K.-P. Huang, W.-J. Hsu, J.-J. Dai, C.-F. Lai, and C.-F. Lin, *Sci. Rep.* **6**, (2016).
- ¹⁰ T. Zhu, Y. Liu, T. Ding, W.Y. Fu, J. Jarman, C.X. Ren, R.V. Kumar, and R.A. Oliver, *Sci. Rep.* **7**, 45344 (2017).
- ¹¹ J.C. Jarman, T. Zhu, P.H. Griffin, and R.A. Oliver, *Jpn. J. Appl. Phys.* **58**, SCCC14 (2019).
- ¹² C.-J. Wang, Y. Ke, G.-Y. Shiu, Y.-Y. Chen, Y.-S. Lin, H. Chen, and C.-F. Lin, *Appl. Sci.* **11**, 8 (2020).
- ¹³ S.-M. Lee, S.-H. Gong, J.-H. Kang, M. Ebaid, S.-W. Ryu, and Y.-H. Cho, *Opt. Express* **23**, 11023 (2015).
- ¹⁴ S.M. Mishkat-Ui-Masabih, A.A. Aragon, M. Monavarian, T.S. Luk, and D.F. Feezell, *Appl. Phys. Express* **12**, 036504 (2019).
- ¹⁵ R.T. ElAfandy, J.-H. Kang, B. Li, T.K. Kim, J.S. Kwak, and J. Han, *Appl. Phys. Lett.* **117**, 011101 (2020).
- ¹⁶ K.J. Lee, S. Oh, S.-J. Kim, S.-Y. Yim, N. Myoung, K. Lee, J.S. Kim, S.H. Jung, T.-H. Chung, and S.-J. Park, *Nanotechnology* **30**, 415301 (2019).
- ¹⁷ M. Mynbaeva, A. Titkov, A. Kryzhanovski, I. Kotousova, A.S. Zubrilov, V.V. Ratnikov, V.Y. Davydov, N.I. Kuznetsov, K. Mynbaev, D.V. Tsvetkov, S. Stepanov, A. Cherenkov, and V.A. Dmitriev, *MRS Internet J. Nitride Semicond. Res.* **4**, (1999).
- ¹⁸ H. Hartono, C.B. Soh, S.J. Chua, and E.A. Fitzgerald, *J. Electrochem. Soc.* **154**, H1004 (2007).
- ¹⁹ S.S. Pasayat, C. Gupta, M.S. Wong, Y. Wang, S. Nakamura, S.P. Denbaars, S. Keller, and U.K. Mishra, *Appl. Phys. Lett.* **116**, 111101 (2020).
- ²⁰ S.S. Pasayat, R. Ley, C. Gupta, M.S. Wong, C. Lynsky, Y. Wang, M.J. Gordon, S. Nakamura, S.P. Denbaars, S. Keller, and U.K. Mishra, *Appl. Phys. Lett.* **117**, 061105 (2020).
- ²¹ S.S. Pasayat, C. Gupta, M.S. Wong, R. Ley, M.J. Gordon, S.P. DenBaars, S. Nakamura, S. Keller, and U.K. Mishra, *Appl. Phys. Express* **14**, 011004 (2021).
- ²² A.P. Vajpeyi, S. Tripathy, S.J. Chua, and E.A. Fitzgerald, *Phys. E Low-Dimens. Syst. Nanostructures* **28**, 141 (2005).
- ²³ D. Chen, H. Xiao, and J. Han, *J. Appl. Phys.* **112**, 064303 (2012).
- ²⁴ C. Zhang, G. Yuan, A. Bruch, K. Xiong, H.X. Tang, and J. Han, *J. Electrochem. Soc.* **165**, E513 (2018).

- ²⁵ Chia-Feng Lin, Kuei-Ting Chen, Chun-Min Lin, and Chung-Chieh Yang, *IEEE Electron Device Lett.* **30**, 1057 (2009).
- ²⁶ H.J. Quah, N.M. Ahmed, Z. Hassan, and W.F. Lim, *J. Electrochem. Soc.* **163**, H642 (2016).
- ²⁷ X. Li, Y.-W. Kim, P.W. Bohn, and I. Adesida, *Appl. Phys. Lett.* **80**, 980 (2002).
- ²⁸ P. Pandey, M. Sui, M.-Y. Li, Q. Zhang, S. Kunwar, J. Wu, Z.M. Wang, G.J. Salamo, and J. Lee, *Cryst. Growth Des.* **16**, 3334 (2016).
- ²⁹ Y.-H. Yeh, K.-M. Chen, Y.-H. Wu, Y.-C. Hsu, and W.-I. Lee, *J. Cryst. Growth* **314**, 9 (2011).
- ³⁰ K. Matsumoto, T. Ono, Y. Honda, T. Yamamoto, S. Usami, M. Kushimoto, S. Murakami, and H. Amano, *Phys. Status Solidi B* **255**, 1700387 (2018).
- ³¹ J. Yu, L. Zhang, J. Shen, Z. Xiu, and S. Liu, *CrystEngComm* **18**, 5149 (2016).
- ³² B. Damilano, S. Vézian, and J. Massies, *Phys. Status Solidi B* 1700392 (2017).
- ³³ B. Damilano, S. Vézian, and J. Massies, *Opt. Express* **25**, 33243 (2017).
- ³⁴ T.H. Ngo, B. Gil, T.V. Shubina, B. Damilano, S. Vézian, P. Valvin, and J. Massies, *Sci. Rep.* **8**, 15767 (2018).
- ³⁵ F. Semond, Y. Cordier, N. Grandjean, F. Natali, B. Damilano, S. Vézian, and J. Massies, *Phys. Status Solidi A* **188**, 501 (2001).
- ³⁶ A. Le Louarn, S. Vézian, F. Semond, and J. Massies, *J. Cryst. Growth* **311**, 3278 (2009).
- ³⁷ S. Sergent, B. Damilano, S. Vézian, S. Chenot, M. Takiguchi, T. Tsuchizawa, H. Taniyama, and M. Notomi, *ACS Photonics* **6**, 3321 (2019).
- ³⁸ S. Fernández-Garrido, T. Auzelle, J. Lähnemann, K. Wimmer, A. Tahraoui, and O. Brandt, *Nanoscale Adv.* **1**, 1893 (2019).
- ³⁹ B. Damilano, P.-M. Coulon, S. Vézian, V. Brändli, J.-Y. Duboz, J. Massies, and P.A. Shields, *Appl. Phys. Express* **12**, 045007 (2019).
- ⁴⁰ S. Sergent, B. Damilano, S. Vézian, S. Chenot, T. Tsuchizawa, and M. Notomi, *Appl. Phys. Lett.* **116**, 223101 (2020).
- ⁴¹ P.-M. Coulon, B. Damilano, B. Alloing, P. Chausse, S. Walde, J. Enslin, R. Armstrong, S. Vézian, S. Hagedorn, T. Wernicke, J. Massies, J. Zúñiga-Pérez, M. Weyers, M. Kneissl, and P.A. Shields, *Microsyst. Nanoeng.* **5**, (2019).
- ⁴² T. Takeuchi, S. Sota, M. Katsuragawa, M. Komori, H. Takeuchi, H. Amano, and I. Akasaki, *Jpn. J. Appl. Phys.* **36**, L382 (1997).
- ⁴³ B. Gil, *Physics of Wurtzite Nitrides and Oxides: Passport to Devices* (Springer, Cham, 2014).
- ⁴⁴ C.-H. Teng, L. Zhang, H. Deng, and P.-C. Ku, *Appl. Phys. Lett.* **108**, 071104 (2016).
- ⁴⁵ Y. Narukawa, M. Ichikawa, D. Sanga, M. Sano, and T. Mukai, *J. Phys. Appl. Phys.* **43**, 354002 (2010).
- ⁴⁶ V. Potin, P. Ruterana, G. Nouet, R.C. Pond, and H. Morkoç, *Phys. Rev. B* **61**, 5587 (2000).
- ⁴⁷ F.C.-P. Massabuau, P.H. Griffin, H.P. Springbett, Y. Liu, R.V. Kumar, T. Zhu, and R.A. Oliver, *APL Mater.* **8**, 031115 (2020).
- ⁴⁸ F.C.-P. Massabuau, H.P. Springbett, G. Divitini, P.H. Griffin, T. Zhu, and R.A. Oliver, *Materialia* **12**, 100798 (2020).
- ⁴⁹ C. Zhao, T.K. Ng, A. Prabaswara, M. Conroy, S. Jahangir, T. Frost, J. O'Connell, J.D. Holmes, P.J. Parbrook, P. Bhattacharya, and B.S. Ooi, *Nanoscale* **7**, 16658 (2015).
- ⁵⁰ P. Varadhan, H.-C. Fu, D. Priante, J.R.D. Retamal, C. Zhao, M. Ebaid, T.K. Ng, I. Ajia, S. Mitra, I.S. Roqan, B.S. Ooi, and J.-H. He, *Nano Lett.* **17**, 1520 (2017).